Computers and Geotechnics 116 (2019) 103197

Contents lists available at ScienceDirect

Computers and Geotechnics

journal homepage: www.elsevier.com/locate/compgeo

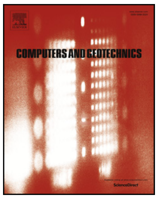

Research Paper

Two-dimensional and three-dimensional inherent fabric in cross-anisotropic granular soils

Quan Sun, Junxing Zheng*

Department of Civil, Construction and Environmental Engineering, Iowa State University, Ames, IA 50011, USA

ARTICLE INFO

Keywords:
Inherent fabric
Cross-anisotropy
Granular soils
X-ray CT
Image processing

ABSTRACT

This paper characterizes fabric anisotropy of granular soils by using both two-dimensional (2D) and three-dimensional (3D) images and evaluates the accuracy and effectiveness of using 2D images to characterize fabric anisotropy in 3D soils. The X-ray computed tomography (X-ray CT) is used to reconstruct the 3D volumetric images of five air-pluviated sand specimens. Then, six slices are obtained by vertically cutting the 3D volumetric image in an angle increment of 30°. The 3D and 2D images are analyzed to determine long axis fabric, contact normal fabric, and branch vector fabric. The results show that 2D images produce satisfactory predictions for long axis fabric and branch vector fabric. The 2D images produce satisfactory predictions for contact normal fabric for rounded to well-rounded sands, but underestimate or contain large uncertainties to predict contact normal fabric for very angular to sub-rounded soils. This study shows that particle shapes affect the inherent fabric anisotropy in sands. Elongated sands tend to have stronger degrees of long axis and branch vector fabric anisotropy. Angular sands tend to have stronger degrees of contact normal fabric anisotropy.

1. Introduction

In natural sedimentary soils, particles depositing through water and air generally align their largest projected surface normal to the depositional direction. As such, cross-anisotropic fabric develops in alluvial, coastal, and lacustrine deposits [1,2]. The deposit direction is defined as fabric direction in this study. Therefore, macro-mechanical behavior of soils depends on the relative angles between loading and fabric directions.

The laboratory test results show that when angles between loading and fabric directions change from zero to 90°, friction angle of sands would typically decrease by 4–16° [3–7], bearing capacity would typically decrease by 25–34% [8], and shear modulus, constrained modulus, and elastic modulus would typically decrease by 20–30% [9]. These studies demonstrated the importance of fabric anisotropy on the mechanical behavior of granular soils.

Fabric can be quantified by spatial distributions of particle long axes, contact normals and branch vectors [10,11], as shown in Fig. 1. In this research, results of three types of fabric characterizations are defined as long axis fabric, contact normal fabric, and branch vector fabric, respectively. Researchers have been using both two-dimensional (2D) and three-dimensional (3D) images of sand specimens to quantify three types of fabrics.

In early works, Oda [4] and Oda and Nakayama [11] injected resin into the pores of sand specimens to solidify them and then cut them into thin sections. They manually traced the orientations of particles' long axes to determine spatial distributions of particle long axes to quantify long axis fabric anisotropy in sands. Later, Kuo et al. [12] and Yang et al. [13] used the same method to cut sand specimen as Oda [4] and Oda and Nakayama [11] did. However, instead of using manual methods to trace particle long axes, they developed image processing techniques to automate such process. The key steps of the image processing method included a thresholding technique to separate particles and resins, and an image segmentation technique to separate contacting particles. These techniques pioneered the development of image-based fabric characterization methodologies. However, their techniques had limitations. Particles must have a different coloration than the background resin. It was very challenging to adequately define the boundaries of individual particles and correctly segment contacting particles in natural soil images.

To address these limitations, Zheng and Hryciw [1,2] proposed a rotational Haar wavelet technique to quantify fabric from particle assembly images. This technique eliminated resin impregnation, specimen cutting, image thresholding, and image segmentation processes. This technique analyzed texture patterns of particle assembly images to determine particle long axes orientation. This technique can rapidly

---

* Corresponding author.
E-mail addresses: quansun@iastate.edu (Q. Sun), junxing@iastate.edu (J. Zheng).

https://doi.org/10.1016/j.compgeo.2019.103197
Received 19 January 2019; Received in revised form 20 June 2019; Accepted 1 August 2019

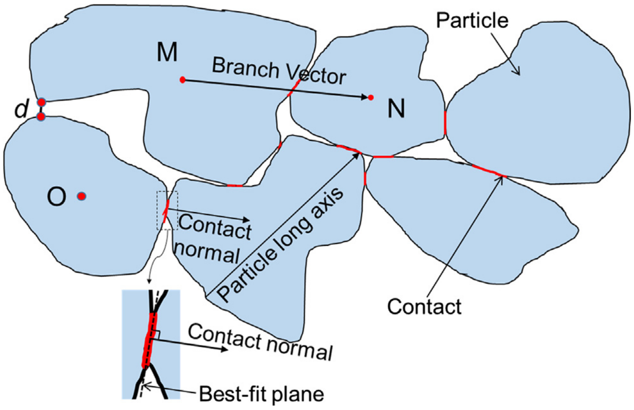

Fig. 1. Schematic graph of directional parameters for fabric characterizations.

and accurately quantify cross-anisotropic fabric based on one cross-section to infer fabric in 3D sand specimens, which significantly facilitates fabric characterization.

To characterize fabric in 3D sand specimens, the X-ray computed tomography (X-ray CT) must be used to scan the specimen and reconstruct the microstructure. Fonseca [10,14] used X-ray CT to investigate evolutions of three types of fabrics (i.e., long axis fabric, contact normal fabric, and branch vector fabric) in sands in triaxial tests. Alam et al. [15] and Imseeh et al. [16], and Al Mahbub and Haque [17] used X-ray CT to investigate evolutions of three types of fabric in sands in oedometer tests. Soriano et al. [18] used X-ray CT to analyze the contact normal fabric of fiber-reinforced sands. Druckrey et al. [19] used X-ray CT to analyze contact normal fabric in sands. Wiebicke [20,21] used X-ray CT to analyze long axis and contact normal fabrics. Recently, Sun [22] developed a series of computational geometry techniques to analyze volumetric images to determine three types of fabrics.

X-ray CT is an ideal technique to characterize fabric in 3D sand specimens. However, the shortcomings of X-ray CT are apparent. First, the initial cost of an X-ray CT device is very high, and an experienced technician is required to operate and maintain it. Second, because of constraints of resolution and field of view, the X-ray CT can only scan a small specimen. The scanned specimen sizes reported in the literature [19,23–27] are typically 12 mm in diameter and 24 mm in height. Therefore, X-ray CT can only be used to investigate fabric in uniform fine sands. Third, processing X-ray CT images is computationally demanding and time-consuming requiring high-performance computing resources. Fourth, extensive imaging processing skills and specialized software are required for analyzing X-ray CT images, which are usually not familiar to geotechnical engineers. Therefore, 3D fabric characterizations are limited to only a few high-end research laboratories; and it has not been used in practice by common soil laboratories.

Due to limitations of X-ray CT techniques, researchers have been cutting 3D specimens into 2D slices and analyzing 2D images to infer fabric in 3D sand specimen [1,2,5,12,13,28–30]. The results may not be accurate compared with 3D fabric characterizations based on X-ray CT techniques, but 2D images have advantages. First, it is simple and can be implemented using off-the-shelf cameras without high-cost X-ray CT. Second, by using good cameras, this method can analyze a large specimen without constraints of field of view and resolution. Third, this method does not require extensive computations and complicated image processing skills. However, the accuracy and effectiveness of fabric characterizations based on 2D images for predicting 3D fabric in cross-anisotropic granular soils are unknown.

This study will use both 2D and 3D images to quantify fabric anisotropy of five sand specimens in the dense condition: crushed limestone (very sand to angular particles), Agsco sand (sub-angular particles), griffin sand (sub-angular to sub-rounded particles), Ottawa sand (rounded to well-rounded particles) and glass beads (well-rounded particles). The 2D and 3D fabric characterizations will be compared to evaluate the effectiveness of the 2D fabric characterizations for predicting 3D fabric characterizations. This study may help researchers and practitioners to decide which characterization methodologies (i.e., simple but less accurate 2D method or complicated but accurate 3D method) should be used in their analyses.

Particle shape significantly affects macro-mechanical behavior of coarse-grained granular soils. Elongated and angular particles can interlock with each other to form larger coordination number and the stronger load-bearing skeleton of granular soils. Experimental and numerical studies have shown that elongated and angular soils exhibit larger index void ratios, a larger angle of internal friction, a larger dilatancy, a larger constant volume friction angle, and a larger small-strain modulus than spherical and rounded soils [1,31–43]. Based on fabric characterizations of five sands with a range of particle shapes, the second goal of this paper is to investigate the effects of particle shape on the fabric anisotropy in sands.

2. Fabric characterization and visualization

2.1. 3D fabric tensor

Spatial orientations of particle long axes, contact normals, and branch vectors are quantified by a second-order fabric tensor φ_{ij}^* [44,45]:

$$\varphi_{ij}^* = \frac{1}{N^*}\sum_{N^*} n_i^* n_j^*, \quad (i, j = 1, 2, 3) \tag{1}$$

where the superscript * represents either ‘p’, ‘c’ or ‘b’ meaning particle long axes, contact normals or branch vectors, respectively; n_i^* (i = 1, 2, 3) are the components of a 3D unit vector $\boldsymbol{n}^*$, which could be a particle long axis (* = p), a branch vector (* = b) or a contact normal (* = c); N^* is the total number of vectors $\boldsymbol{n}^*$ in the assembly of particles.

Eq. (1) yields a 3-by-3 symmetric matrix. The principal values (i.e., eigenvalues) of the fabric tensor, defined as φ_1^*, φ_2^*, and φ_3^*, are commonly used to perform advanced geotechnical analysis, such as the development of anisotropic constitutive models [46–50] and analysis of DEM results [51–55]. For natural sedimentary soils exhibiting cross-anisotropic fabric, as shown in Fig. 2(a), φ_2^*, and φ_3^* should be very close to each other. The φ_1^* is the fabric direction ($\boldsymbol{F}$ in Fig. 2(a)), which should be close to the vertical direction. The angle between $\boldsymbol{F}$ and the horizontal plane is defined as β, which should be close to 90°. For cross-anisotropic fabric, the single parameter β can be used to quantify fabric direction relative to the horizontal plane.

2.2. 3D rose diagram and density function

Orientations of particle long axes, contact normals and branch vectors in 3D space can be visualized by a rose diagram. For example, this paper generates a random distribution of vectors in 3D space. These vectors are plotted as a 3D rose diagram in Fig. 3(a). Each bar represents the frequency of vectors in this direction in the 3D space.

The 3D rose diagram can be represented by a 3D density function $f(n)$ [45]:

$$f(n) = \frac{1}{2\pi}\left(1 + D_{ij}^* n_i^* n_j^* + D_{ijkl}^* n_i^* n_j^* n_k^* n_l^*\right), \quad (i, j, k, l = 1, 2, 3) \tag{2}$$

where D_{ij}^* is the second-order deviatoric fabric tensor and D_{ijkl}^* is the fourth-order deviatoric fabric tensor:

$$D_{ij}^* = \frac{2}{15}\left(\varphi_{ij}^* - \frac{1}{3}\delta_{ij}\right), \quad (i, j = 1, 2, 3) \tag{3}$$

$$D_{ijkl}^* = \frac{2}{15}\left(\varphi_{ijkl}^* - \frac{6}{7}\delta_{(ij}\varphi_{kl)}^* + \frac{3}{35}\delta_{(ij}\delta_{kl)}\right), \quad (i, j, k, l = 1, 2, 3). \tag{4}$$

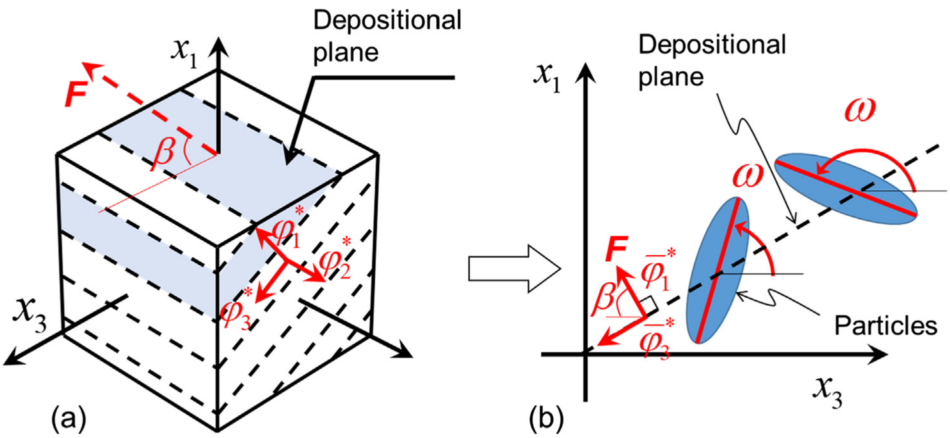

Fig. 2. Fabric characterizations by 3D and 2D images: (a) Cross anisotropic fabric in 3D soil specimen; and (b) 2D fabric characterization in one slice to estimate fabric anisotropy in 3D soil specimen.

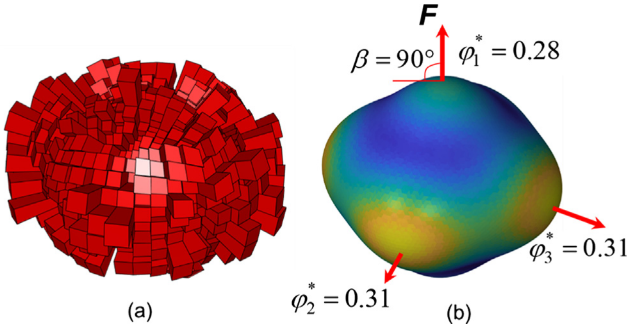

Fig. 3. Fabric visualization: (a) 3D rose diagram; and (b) 3D density function $f(n)$.

In Eqs. (2) and (3), the δ_{ij} is the Kronecker delta and the φ_{ij}^* and φ_{ijkl}^* are the second-order and the fourth-order fabric tensors, respectively. The second-order fabric tensor is defined in Eq. (1). The fourth-order fabric tensor is defined as:

$$\varphi_{ijkl}^* = \frac{1}{N^*}\sum_{N^*} n_i^* n_j^* n_k^* n_l^*, \quad (i,j,k,l = 1, 2, 3), \tag{5}$$

The vectors in Fig. 3(a) are used to determine the density function by using Eqs. (1)–(5). The result is shown in Fig. 3(b). The density function is essentially a best-fitting surface of the 3D rose diagram. The previously defined principal values (i.e. φ_1^*, φ_2^*, and φ_3^*) and fabric direction (***F*** and β) are computed using Eq. (1) and superimposed on the 3D density function in Fig. 3(b).

2.3. 2D fabric tensor

In the cross-anisotropic granular soils in Fig. 2(a), the particles develop isotropic fabric in the depositional plane, and therefore, φ_2^* and φ_3^* should be the same [2,11]. Therefore, we only need to analyze one slice in the x_1–x_3 plane to determine three principal values of φ_1^*, φ_2^*, and φ_3^*, as shown in Fig. 2(b). Based on this concept, Oda and Nakayama [11] developed the fabric characterization method based on 2D images.

In the x_1–x_3 plane in Fig. 2(b), Eq. (1) is simplified as a 2D fabric tensor (the bar on the top indicates it is a 2D fabric tensor):

$$\bar{\varphi}_{ij}^* = \frac{1}{N^*}\sum_{N^*} \bar{n}_i^* \bar{n}_j^*, \quad (i,j = 1, 2) \tag{6}$$

where $\bar{n}_i^*$ $(i = 1, 2)$ are the components of a 2D unit vector $\bar{\boldsymbol{n}}^*$. Eq. (6) is a 2-by-2 matrix having two principal values of $\bar{\varphi}_1^*$ and $\bar{\varphi}_3^*$.

Assuming that the principal values $\bar{\varphi}_1^*$ and $\bar{\varphi}_3^*$ in a 2D image are proportional to the principal values φ_1^* and φ_3^* in a 3D image [11] and knowing that $\varphi_2^* = \varphi_3^*$ (for cross-anisotropy) and $\varphi_1^* + \varphi_2^* + \varphi_3^* = 1$, the principal values of the fabric tensor φ_1^*, φ_2^*, and φ_3^* in 3D sands can be obtained as:

$$\varphi_1^* = \frac{1 - \bar{\varphi}_1^* + \bar{\varphi}_3^*}{3 + \bar{\varphi}_1^* - \bar{\varphi}_3^*}, \quad \varphi_2^* = \varphi_3^* = \frac{1 + \bar{\varphi}_1^* - \bar{\varphi}_3^*}{3 + \bar{\varphi}_1^* - \bar{\varphi}_3^*}, \tag{7}$$

The fabric direction ***F*** is the eigenvector of $\bar{\varphi}_1^*$, and the angle between ***F*** and the horizontal plane is β as shown in Fig. 2(b). Therefore, by analyzing one slice of the cross-anisotropic specimen, the 3D fabric characterizations, including φ_1^*, φ_2^*, φ_3^* and β, can also be determined.

2.4. 2D rose diagram and density function

Orientations of particle long axes, contact normal, and branch vectors in the 2D plane can be plotted as a 2D rose diagram, as shown in Fig. 4.

The 2D rose diagram can be quantified by a 2D density function [45]:

$$\bar{f}(n) = \frac{1}{2\pi}(1 + \bar{D}_{ij}^* \bar{n}_i^* \bar{n}_j^* + \bar{D}_{ijkl}^* \bar{n}_i^* \bar{n}_j^* \bar{n}_k^* \bar{n}_l^*), \quad (i,j,k,l = 1, 2), \tag{8}$$

The second-order deviatoric fabric tensor $\bar{D}_{ij}^*$ and the fourth-order deviatoric fabric tensor $\bar{D}_{ijkl}^*$ from 2D images are

$$\bar{D}_{ij}^* = 4\left(\bar{\varphi}_{ij}^* - \frac{1}{2}\delta_{ij}\right), \quad (i,j = 1, 2), \tag{9}$$

$$\bar{D}_{ijkl}^* = 16\left(\bar{\varphi}_{ijkl}^* - \delta_{(ij}\bar{\varphi}_{kl)}^* + \frac{1}{8}\delta_{(ij}\bar{\varphi}_{kl)}^*\right), \quad (i,j = 1, 2), \tag{10}$$

In Eqs. (9) and (10), the δ_{ij} is the Kronecker delta; the $\bar{\varphi}_{ij}^*$ can be computed from Eq. (6). The $\bar{\varphi}_{ijkl}^*$ is the fourth-order fabric tensor in 2D images:

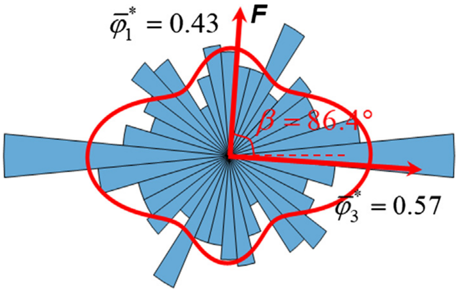

Fig. 4. The 2D rose diagram and 2D density function $f(n)$.

$$\bar{\varphi}^{*}_{ijkl} = \frac{1}{N^{*}} \sum_{N^{*}} \bar{n}_i^{*}\bar{n}_j^{*}\bar{n}_k^{*}\bar{n}_l^{*}, \quad (i, j, k, l = 1, 2), \tag{11}$$

The vectors in Fig. 4 are used to determine the 2D density function by using Eqs. (8)–(11). The density function is superimposed as the curve in Fig. 4, which is essentially a best-fitting curve of the 2D rose diagram. The previously defined principal values (i.e. $\bar{\varphi}_1^{*}$ and $\bar{\varphi}_3^{*}$) and fabric direction ($\boldsymbol{F}$ and β) are also superimposed on the 2D density function in Fig. 4.

2.5. *Degree of fabric anisotropy*

To quantify the degree of fabric anisotropy of 3D soil specimens, Barreto and O'Sullivan [55] proposed a generalized octahedral fabric factor:

$$\Delta^{*}_{3D} = \frac{1}{\sqrt{2}}[(\varphi_1^{*} - \varphi_2^{*})^2 + (\varphi_1^{*} - \varphi_3^{*})^2 + (\varphi_2^{*} - \varphi_3^{*})^2]^{0.5} \tag{12}$$

where the superscript * represents either 'p', 'c' or 'b' meaning degrees of long axis fabric anisotropy, contact normals fabric anisotropy, or branch vectors fabric anisotropy, respectively. In 2D fabric characterizations, φ_2^{*} equals to φ_3^{*}. Therefore, the Eq. (12) is simplified as $\Delta^{*}_{2D} = \varphi_1^{*} - \varphi_2^{*}$.

3. 3D and 2D images of soil specimens

3.1. *Soil specimen*

Five sand specimens were used in this study, including crushed limestone (very angular particles), Agsco sand (angular to sub-angular particles), Griffin (subangular to sub-rounded particles), Ottawa sand (rounded to well-rounded particles) and glass beads (well-rounded particles). For each sand, we manually picked 2925 particles in the size range of #30 sieve (0.595 mm) to #16 sieve (1.19 mm). These particles were weighted and then were funneled into a 12 mm diameter plastic cylinder to generate a loose specimen. The designed relative density was 85% for five sand specimens. Therefore, based on the designed relative density, final heights of these five sand specimens in the cylinder were computed as 15.5 mm, 14.0 mm, 13.0 mm, 12.4 mm, and 12.0 mm for crushed limestone, Agsco sand, Griffin sand, Ottawa sand, and glass beads respectively. Then, the cylinder was mounted on a vibration table and was shaken until the specimens reached the designed heights.

3.2. *Improve watershed analysis to identify individual particles*

A high-resolution X-ray CT was used to scan the soil specimen with a spatial resolution of 12 μm/voxel. Having obtained 3D volumetric images, individual soil particles were identified by image segmentation techniques. The first step was to use image thresholding techniques [56] to segment air and particles. This resulted in a binary image, in which the soil particles had a voxel value of ones (white color), and the air had a voxel value of zeros (black color). In this binary image, the soil particles were contacting with each other. Therefore, the second step was to use a watershed analysis [27,57] technique to segment contacting particles.

The watershed analysis cannot discriminate two contacting particles and a peanut-shaped particle, and therefore, mistakenly segmented peanut-shaped particles into two and even more particles [58]. An improved watershed analysis, developed by Sun et al. [22], was used to overcome oversegmentation. The concepts of the watershed analysis and improved watershed analysis are briefly introduced here. Two contacting particles in Fig. 5(a) are used to explain the idea. Particle 1 is a peanut-shaped particle containing two spheres, and particle 2 is a spherical particle.

The watershed analysis contains two steps: distance transform and watershed transform. The distance transform computes the minimum distance of each point inside of the particle to the particle surface, which results in a Euclidean distance map. The Euclidean distance map can be conceptually plotted as a topographic map, as shown in Fig. 5(b). The points with the maximum distance value create local minima while the shallower points between two local minima create ridges. The watershed transform can be thought of as gradually injecting water into basins through the local minima points. The water table rises uniformly and eventually, and the water from the two basins will meet along the ridges. The meeting planes identify the contacts between particles.

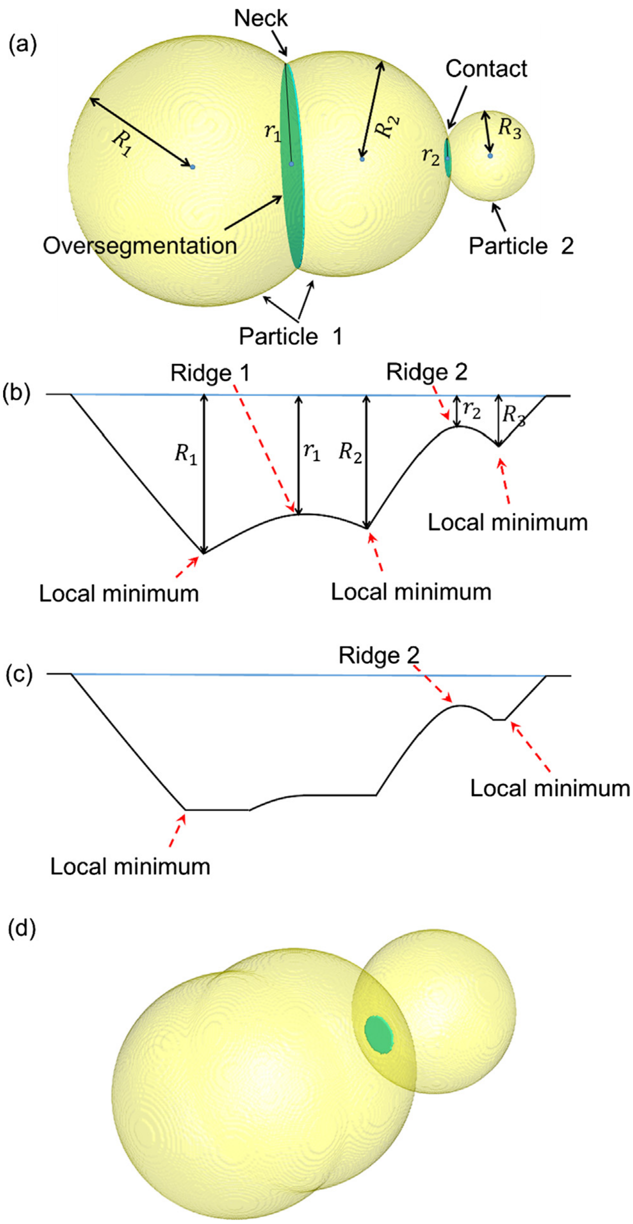

Fig. 5. Illustration of improved watershed analysis: (a) two contacting particles (particle 1 is a peanut-shaped particle and particle 2 is a spherical particle) and oversegmentation of peanut-shaped particle; (b) Euclidean distance map computed by traditional watershed analysis; (c) the modified distance map by image morphological reconstruction technique in the improved watershed analysis; and (d) the correct segmentation by improved watershed analysis.

Each constrained region in the image generates a ridge in the distance map, and watershed analysis essentially identifies these ridges and segment particles at ridges. However, the peanut-shaped particles, such as particle 1, also contain a constrained region, which can be

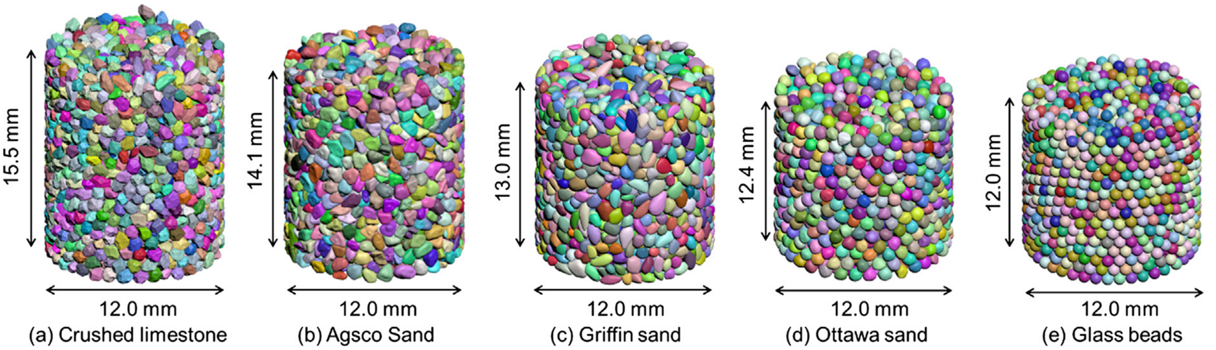

(a) Crushed limestone (b) Agsco Sand (c) Griffin sand (d) Ottawa sand (e) Glass beads

	(a) Crushed limestone	(b) Agsco Sand	(c) Griffin sand	(d) Ottawa sand	(e) Glass beads
S	0.79	0.78	0.70	0.94	1.00
R	0.18	0.35	0.54	0.72	1.00

Fig. 6. Five soil specimens scanned by X-ray CT.

regarded as necks of peanut-shaped particles. The watershed analysis cannot discriminate the necks of peanut-shaped particles and contacts between two particles, leading to oversegmentation of peanut-shaped particles.

To teach a computer to discriminate the necks and real contacts, Sun et al. [22] developed an improved watershed analysis to automatically discriminate neck ridges and contact ridges based on the observation that necks usually had large constraint regions than the contacts. As a result, ridges generated by necks are shallower than ridges generated by contacts. Then, this technique uses an image morphological reconstruction technique to modify the Euclidean distance map by elevating the local minima, so that neck ridges (i.e., the ridge 1 in Fig. 5(b)) are hidden, but contact ridges (i.e., the ridge 2 in Fig. 5(b)) still exist. In the modified distance map in Fig. 5(c), watershed transform performs segmentation only at ridge 2. The correct segmentation result is shown in Fig. 5(d).

The improved watershed analysis was performed on the volumetric image of five sand specimens. The results are shown in Fig. 6 respectively. After segmentation, 2925 particles were identified for each sand, which was the same as the number of used particles during specimen preparation. Therefore, five soils with different particle shapes were correctly segmented, which verified the effectiveness and reliability of the improved watershed analysis.

In the air-pluviated sand specimen, the isotropic fabric develops in a horizontal plane (i.e., deposit plane), and anisotropic fabric develops in the vertical plane (i.e., deposit direction). Therefore, previous studies [1,2,5,12,13,28–30] cut the specimen in the vertical direction and analyzed fabric anisotropy in these 2D images to infer fabric anisotropy in 3D soil specimen based on Eqs. (6) to (11). In this study, six 2D slices were obtained by vertically cutting the 3D volumetric image in an angle increment of 30°. The obtained images are shown in Fig. 7.

3.3. Particle shape characterization

The sphericity and roundness are used to quantify the particle shapes in this study. The sphericity quantifies how closely the overall shape of the particle conforms to a perfect sphere. This study uses the sphericity definition proposed by Krumbein and Sloss [59]:

$$S = \sqrt[3]{\frac{d_2 d_3}{d_1}} \tag{13}$$

where d_1, d_2, and d_3 are particle length, width, and thickness.

The d_1, d_2, and d_3 values can be determined by a principal component analysis technique [19,22]. The points on the 3D particle surfaces are projected onto orthogonal directions. Each direction represents a principal component. The first principal component captures the largest variance of points, which determine the d_1 of the particle. Each succeeding component, in turn, captures the largest variance for the remaining data points under the constraint that it is orthogonal to the preceding components. Therefore, the second and third components identify the d_2 and d_3 of the particle, respectively. The 3D particles in Fig. 6 were analyzed by the principal component analysis. The determined S values for five soils are shown in Fig. 6.

The roundness quantifies the angularity of particles. Based on the maximum projections of particles, the roundness definition was proposed by Wadell [60–62]:

$$R = \frac{\text{Average radius of curvatures of corners}}{\text{Radius of the largest inscribed circle}} = \frac{1}{r_{in}}\left(\frac{1}{N}\sum_{i=1}^{N} r_i\right) \tag{14}$$

where r_i is the radius of the i-th circle fitting to the i-th corner to compute the radius of curvature, N is the total number of corners, and r_{in} is the radius of the maximum inscribed circle.

Zheng and Hryciw [63,64] developed a computational geometry algorithm, which can automatically identify the maximum projections of the particles, identify corners and corner circles, and compute R values. The 3D particles in Fig. 6 were analyzed by the computational geometry code. The determined R values for five soils are shown in Fig. 6.

4. Fabric characterizations from 2D and 3D images for granular soils

This section briefly illustrates image processing techniques to compute particle long axes, contact normals, and branch vectors in 2D and 3D images. The details can refer to Sun et al. [22]. Then, three types of fabrics, namely long axis fabric, contact normal fabric, and branch vector fabric, are determined from both 2D and 3D images based on Eqs. (1)–(12). Then, results from 2D images are compared with results from 3D images in terms of three principal values (i.e. φ_1^*, φ_2^*, and φ_3^*, * = p, c and b), fabric direction (β), rose diagram, density function, and degree of fabric anisotropy (Δ^*). The effects of particle shapes on the degree of fabric anisotropy are investigated.

4.1. Long axis fabric anisotropy

The particle long axes in 3D images (Fig. 6) and 2D images (Fig. 7) can be determined using principal component analysis. The results are shown in Figs. 8 and 9. The glass beads do not have long axes and therefore, are not analyzed here.

The long axes in 3D and 2D images are used to determine principal values (i.e., φ_1^p, φ_2^p, and φ_3^p), fabric direction (β), 3D rose diagram, and density function. The results are shown in Fig. 10. In the air-pluviated soil specimens, particle long axes display a preferred horizontal orientation under the gravity. Therefore, φ_2^p is close to φ_3^p and they are

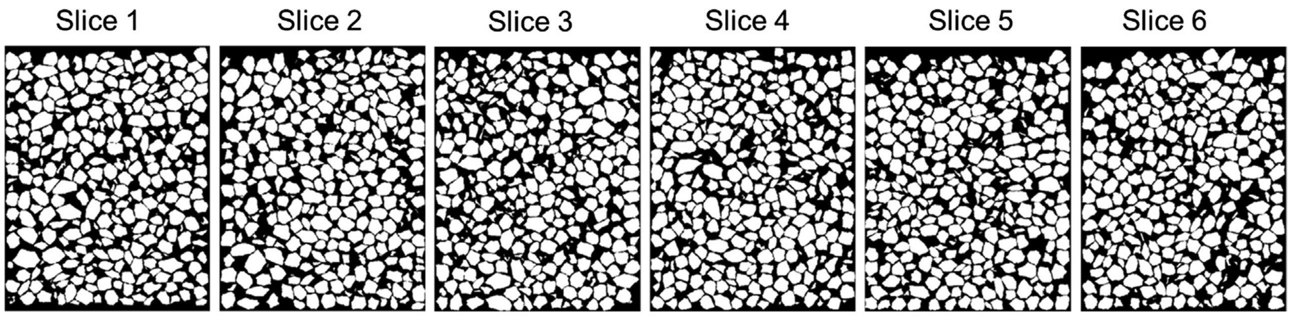

(a) Crushed limestone

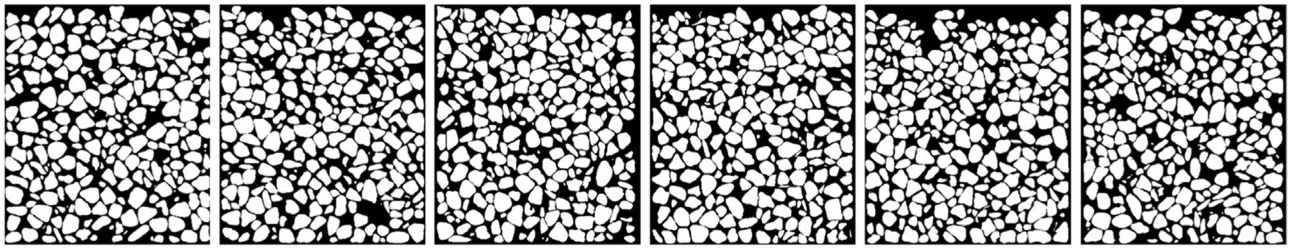

(b) Agsco Sand

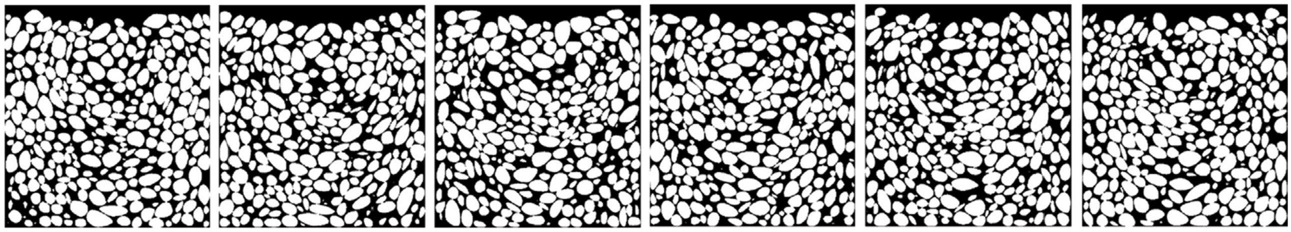

(c) Griffin sand

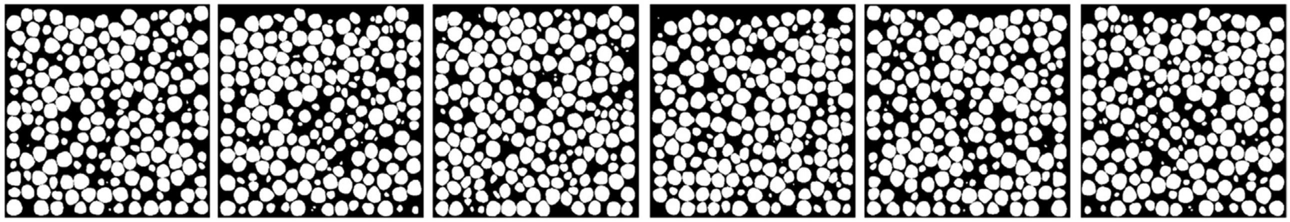

(d) Ottawa sand

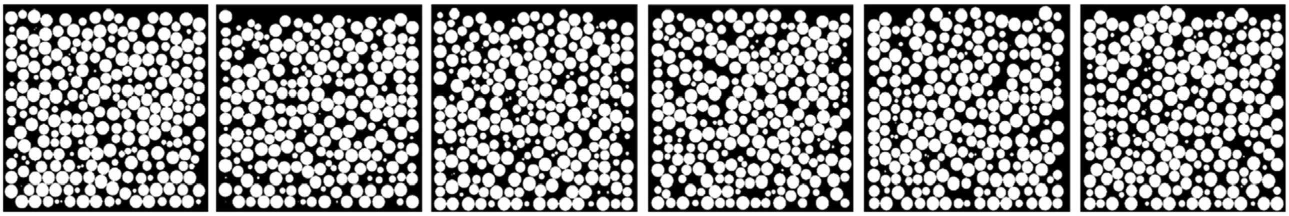

(e) Glass beads

Fig. 7. Six slices by cutting the 3D soil specimens.

larger than φ_1^p, and shapes of 3D and 2D rose diagrams and densities functions are flat in the horizontal direction. The direction of long axis fabric is close to the vertical (gravity) direction with β values close to 90°.

The φ_1^p, φ_2^p and φ_3^p values based on 2D images vary depending on different slicing directions. However, the variance range is small, within 0.05 for these four sands analyzed in this study. The φ_1^p, φ_2^p and φ_3^p values based on 2D images are close to these values based on 3D images, with a maximum divergence of 0.03.

The φ_1^p, φ_2^p and φ_3^p values are used to compute the degrees of contact normal fabric anisotropy (Δ^c) for five sands using Eq. (12). The results are plotted against sphericity and roundness values of four sand in Fig. 11, where the Δ_{3D}^p and Δ_{2D}^p mean Δ^p values are computed from 3D and 2D images, respectively. The Δ_{2D}^p values agree very well with Δ_{3D}^p values with a maximum divergence of 0.05.

In Fig. 11(a), the Δ_{3D}^p decreases as increasing sphericity (less elongated), which indicates the elongated soils tend to develop stronger long axis fabric anisotropy. The same observation has been reported by Zheng and Hryciw [1,2], Lade et al. [65], and Oda [66]. In Fig. 11(b), there is no decisive relationship between Δ_{3D}^p and roundness.

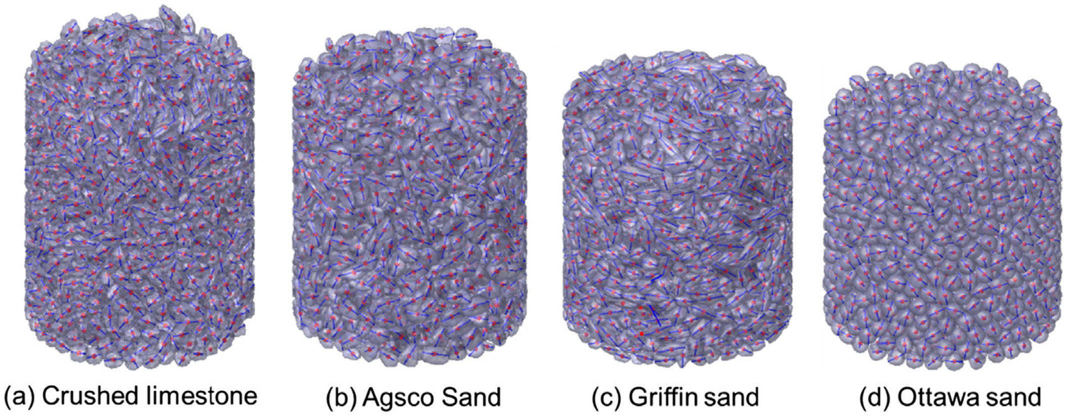

Fig. 8. Particle long axes in 3D images by the principal component analysis.

In summary, the results in Figs. 10 and 11 show that long axis fabric characterizations based on 2D images yield adequately accurate approximations to long axis fabric anisotropy based on 3D images. This confirms the validity of the previous studies [1,2,5,12,13,28–30] using the 2D images to estimate long axis fabric anisotropy in 3D sand specimens.

4.2. Contact normal fabric anisotropy

The contacts in 3D and 2D images can be determined by the

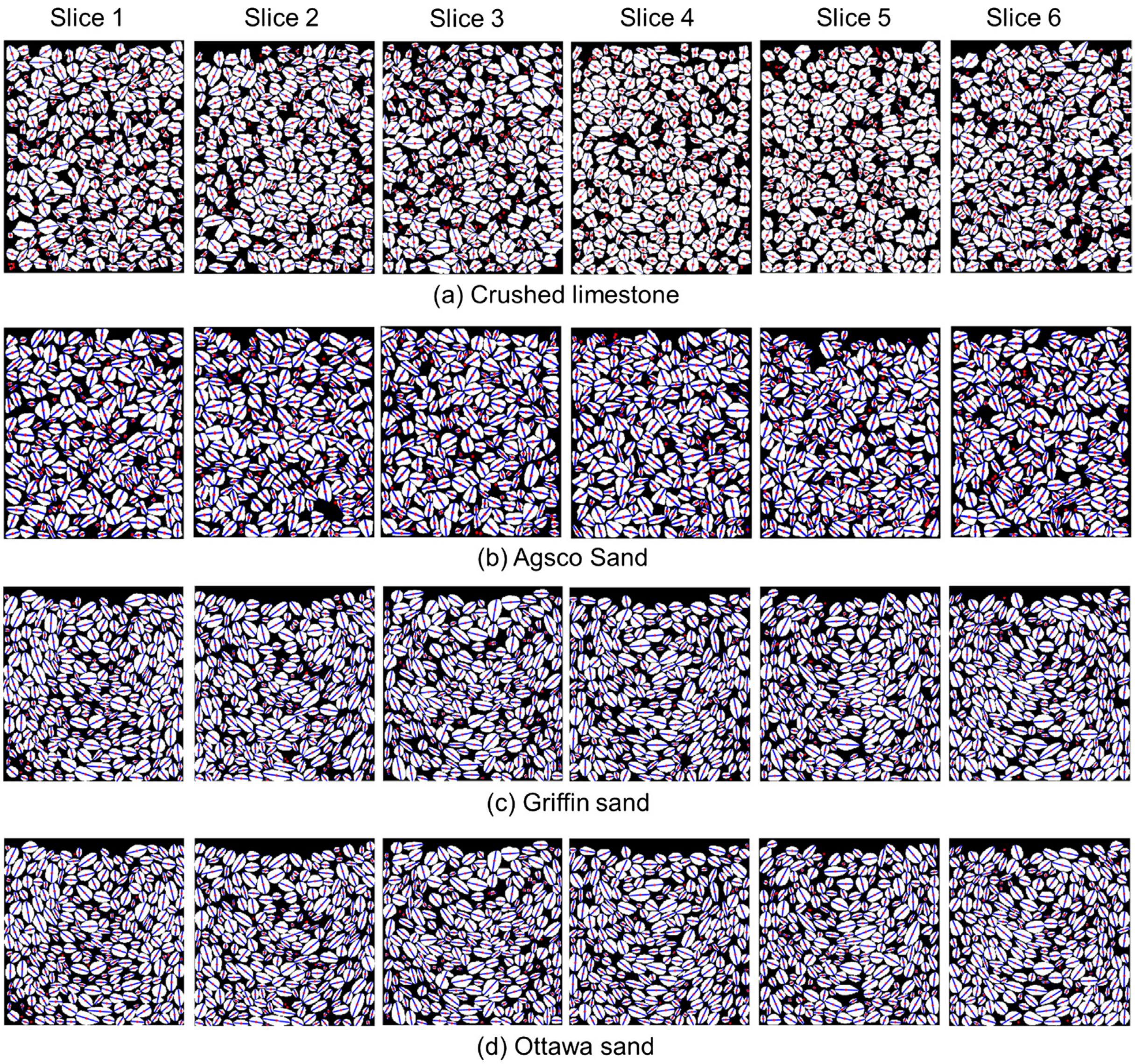

Fig. 9. Particle long axes in 2D images by the principal component analysis.

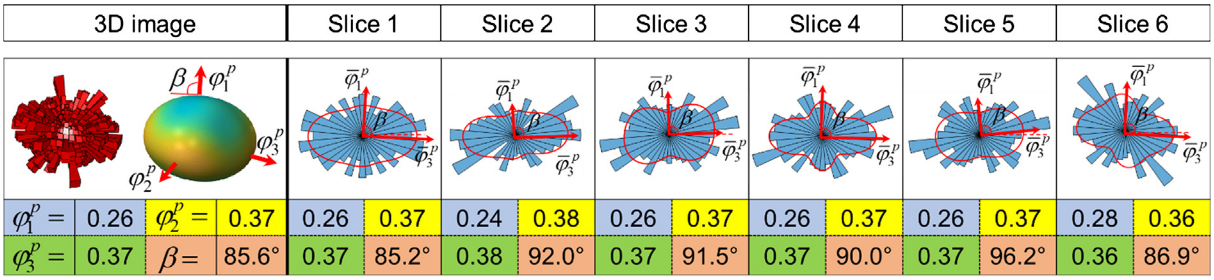

	3D image	Slice 1	Slice 2	Slice 3	Slice 4	Slice 5	Slice 6
$\varphi_1^p =$	0.26	0.26	0.24	0.26	0.26	0.26	0.28
$\varphi_2^p =$	0.37	0.37	0.38	0.37	0.37	0.37	0.36
$\varphi_3^p =$	0.37	0.37	0.38	0.37	0.37	0.37	0.36
$\beta =$	85.6°	85.2°	92.0°	91.5°	90.0°	96.2°	86.9°

(a) Crushed limestone (S = 0.79, R = 0.18)

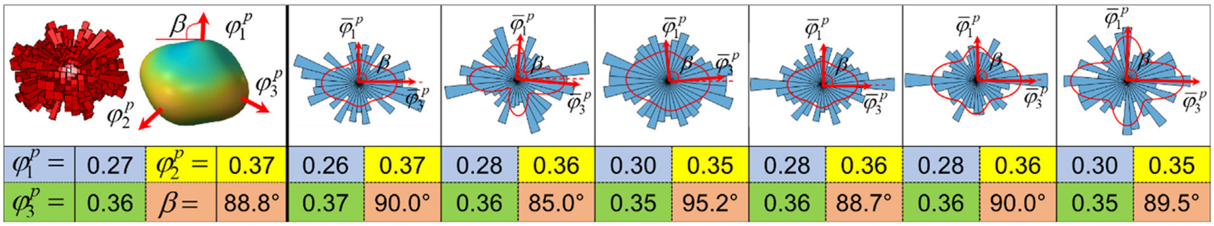

	3D image	Slice 1	Slice 2	Slice 3	Slice 4	Slice 5	Slice 6
$\varphi_1^p =$	0.27	0.26	0.28	0.30	0.28	0.28	0.30
$\varphi_2^p =$	0.37	0.37	0.36	0.35	0.36	0.36	0.35
$\varphi_3^p =$	0.36	0.37	0.36	0.35	0.36	0.36	0.35
$\beta =$	88.8°	90.0°	85.0°	95.2°	88.7°	90.0°	89.5°

(b) Agsco sand (S = 0.78, R = 0.35)

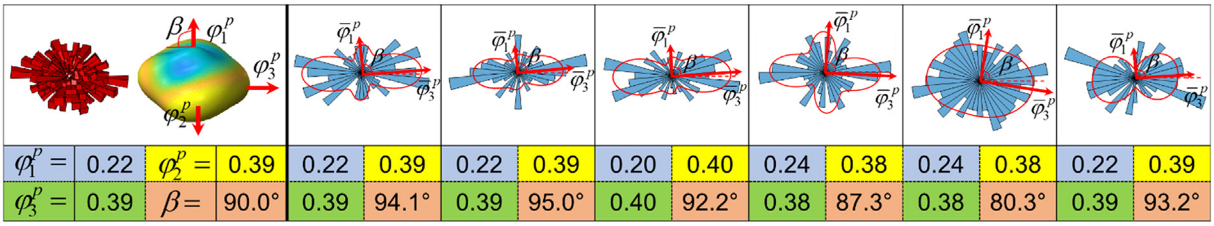

	3D image	Slice 1	Slice 2	Slice 3	Slice 4	Slice 5	Slice 6
$\varphi_1^p =$	0.22	0.22	0.22	0.20	0.24	0.24	0.22
$\varphi_2^p =$	0.39	0.39	0.39	0.40	0.38	0.38	0.39
$\varphi_3^p =$	0.39	0.39	0.39	0.40	0.38	0.38	0.39
$\beta =$	90.0°	94.1°	95.0°	92.2°	87.3°	80.3°	93.2°

(c) Griffin sand (S = 0.70, R = 0.56)

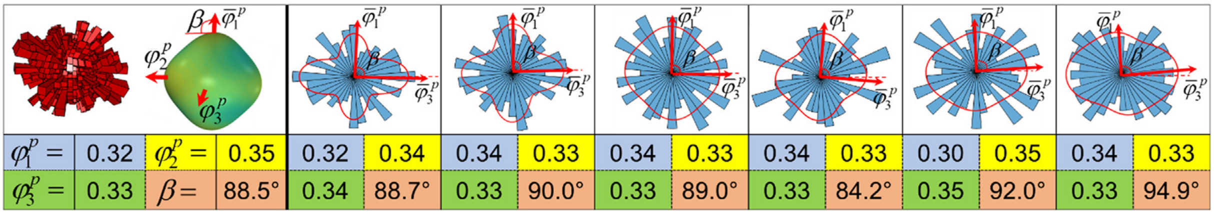

	3D image	Slice 1	Slice 2	Slice 3	Slice 4	Slice 5	Slice 6
$\varphi_1^p =$	0.32	0.32	0.34	0.34	0.34	0.30	0.34
$\varphi_2^p =$	0.35	0.34	0.33	0.33	0.33	0.35	0.33
$\varphi_3^p =$	0.33	0.34	0.33	0.33	0.33	0.35	0.33
$\beta =$	88.5°	88.7°	90.0°	89.0°	84.2°	92.0°	94.9°

(d) Ottawa sand (S = 0.94, R = 0.72)

Legend: $\varphi_1^p =$ 🟦 $\varphi_2^p =$ 🟨 $\varphi_3^p =$ 🟩 $\beta =$ 🟧

Fig. 10. Long axis fabric characterizations based on 2D and 3D images.

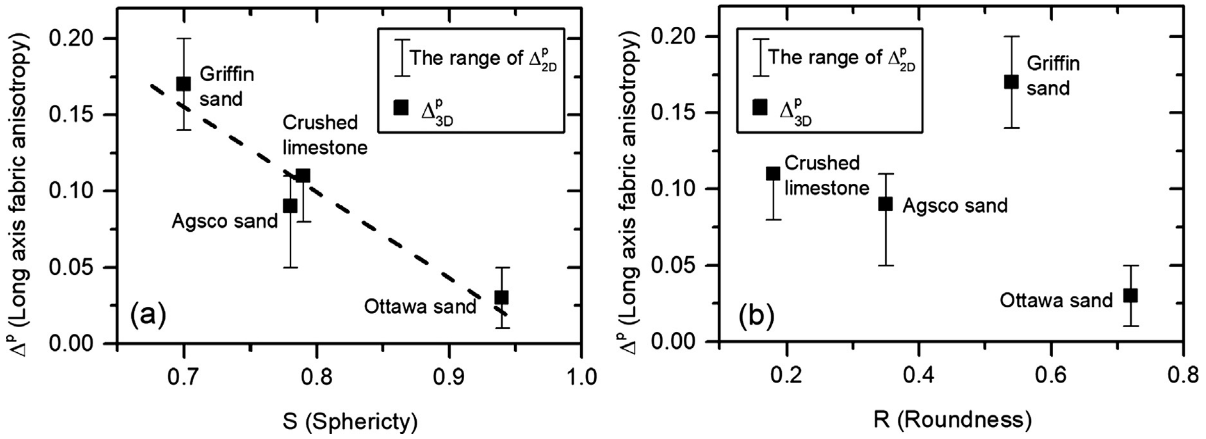

Fig. 11. The degrees of long axis fabric anisotropy from 2D and 3D images and their relationships with soil sphericity and roundness.

improved watershed analysis, as shown in Figs. 12 and 13, respectively. Then, the contact normals can be determined. The contact normals in 2D images are shown in Fig. 13.

The contact normals in the 3D and 2D images are used to determine principal values (i.e. φ_1^c, φ_2^c, and φ_3^c), fabric direction (β), 3D rose diagram, and density function. The results are shown in Fig. 14. Because of the gravity, the particle contact normals display a preferred vertical orientation. Therefore, φ_1^c is larger than φ_2^c and φ_3^c, and shapes of 3D and

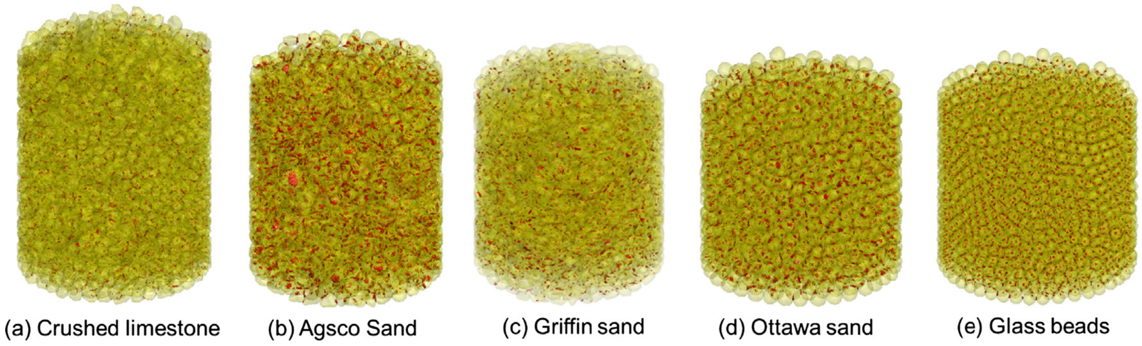

Fig. 12. Contacts in 3D images by the improved watershed analysis.

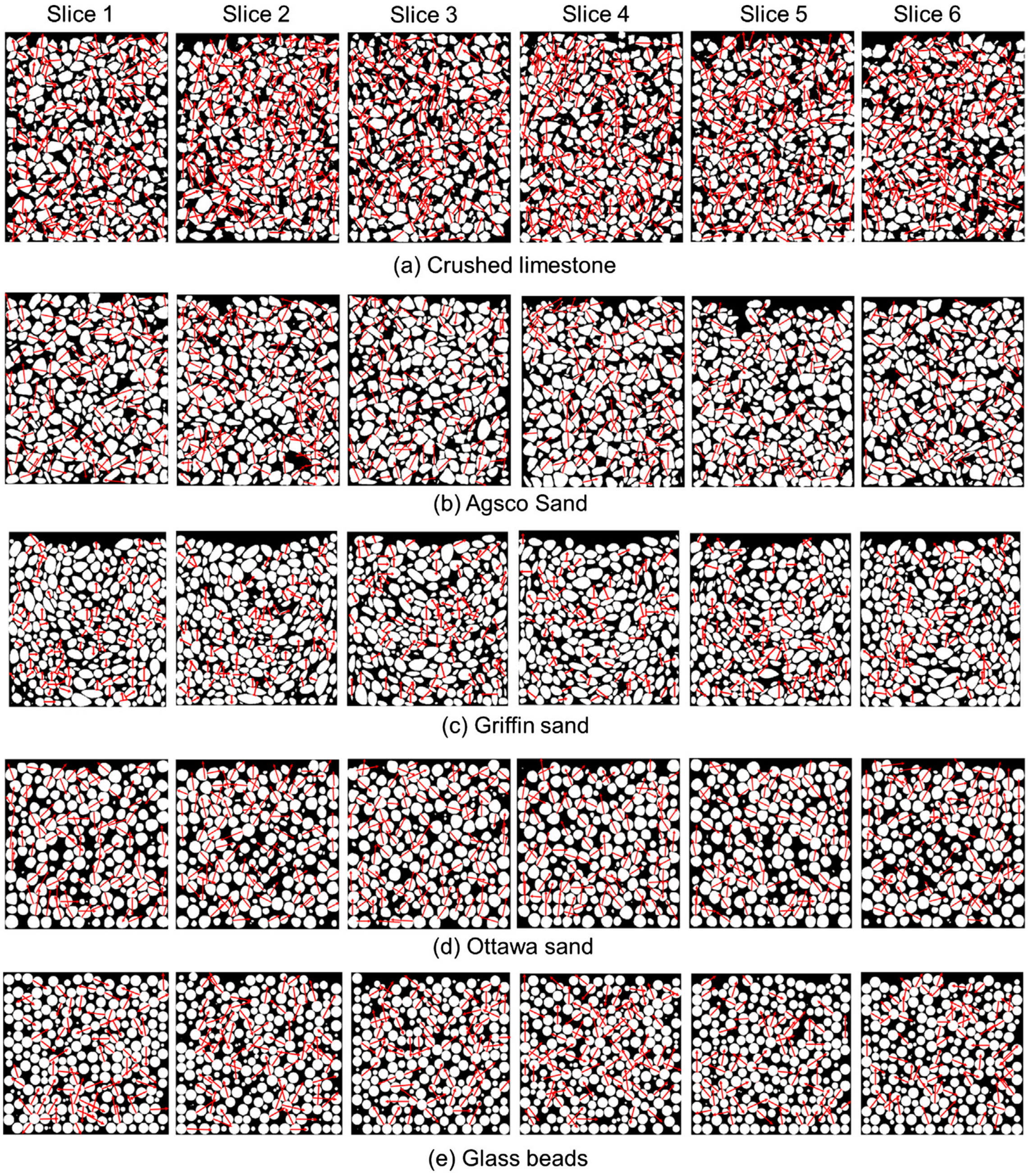

Fig. 13. Contacts in 2D images by the improved watershed analysis.

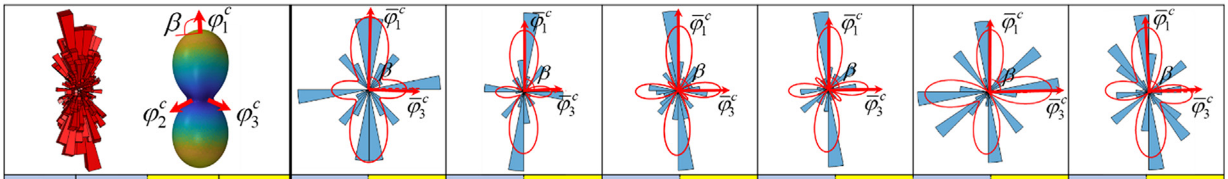

3D image				Slice 1		Slice 2		Slice 3		Slice 4		Slice 5		Slice 6	
$\varphi_1^p =$	0.58	$\varphi_2^p =$	0.21	0.48	0.26	0.50	0.25	0.46	0.27	0.50	0.25	0.34	0.33	0.48	0.26
$\varphi_3^p =$	0.21	$\beta =$	87.9°	0.26	87.6°	0.25	91.7°	0.27	90.0°	0.25	90.0°	0.33	90.0°	0.26	91.0°

(a) Crushed limestone (S = 0.79, R = 0.18)

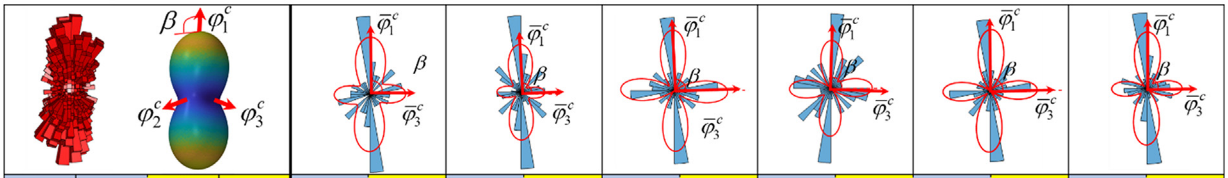

$\varphi_1^p =$	0.51	$\varphi_2^p =$	0.25	0.42	0.29	0.46	0.27	0.38	0.31	0.38	0.31	0.40	0.30	0.42	0.29
$\varphi_3^p =$	0.24	$\beta =$	90.0°	0.29	90.0°	0.27	92.0°	031	91.5°	0.31	87.7°	0.30	90.0°	0.29	90.0°

(b) Agsco sand (S = 0.78, R = 0.35)

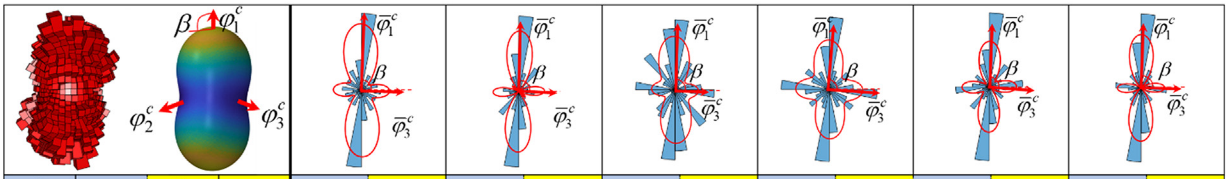

$\varphi_1^p =$	0.45	$\varphi_2^p =$	0.28	0.50	0.25	0.56	0.22	0.48	0.26	0.40	0.30	0.44	0.28	0.52	0.24
$\varphi_3^p =$	0.27	$\beta =$	88.5°	0.25	88.3°	0.22	88.8°	0.26	83.8°	0.30	83.8°	0.28	85.7°	0.24	87.9°

(c) Griffin sand (S = 0.70, R = 0.56)

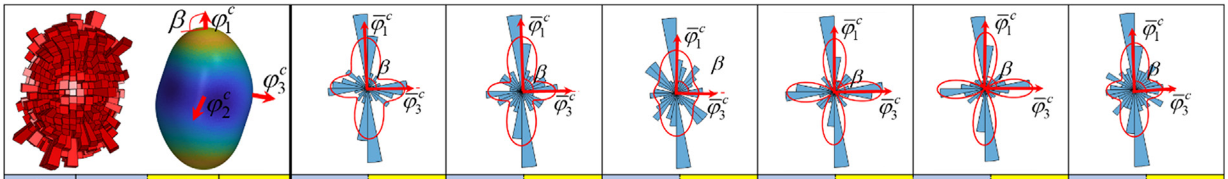

$\varphi_1^p =$	0.38	$\varphi_2^p =$	0.33	0.35	0.30	0.42	0.29	0.42	0.29	0.36	0.32	0.38	0.31	0.42	0.29
$\varphi_3^p =$	0.29	$\beta =$	87.9°	0.30	90.5°	0.29	91.0°	0.29	88.4°	0.32	90.0°	0.31	90.0°	0.29	91.0°

(d) Ottawa sand (S = 0.94, R = 0.72)

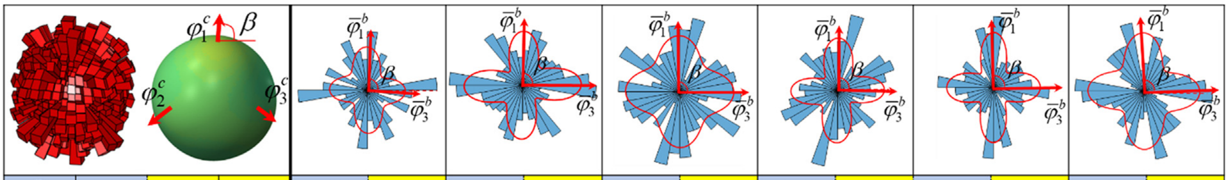

$\varphi_1^p =$	0.34	$\varphi_2^p =$	0.33	0.36	0.32	0.34	0.33	0.36	0.32	0.36	0.32	0.36	0.32	0.34	0.33
$\varphi_3^p =$	0.33	$\beta =$	88.5°	0.32	88.5°	0.33	90.0°	0.32	89.5°	0.32	89.0°	0.32	90.2°	0.33	91.0°

(e) Glass Beads (S = 1.00, R = 1.00)

Legend: $\varphi_1^p =$ 🟦 $\varphi_2^p =$ 🟨 $\varphi_3^p =$ 🟩 $\beta =$ 🟧

Fig. 14. Contact normal fabric characterizations based on 2D and 3D images.

2D rose diagrams and density functions are elongated in the vertical direction. The direction of contact normal fabric is vertical with β values close to 90°.

As shown in Fig. 14, the φ_1^c, φ_2^c and φ_3^c values based on 2D images have a large variance range depending on slicing directions for crushed limestone, Agsco sand, and Griffin sand (from very angular to subrounded sands). The maximum variance range is 0.16 for these three sands. For Ottawa sand and Glass beads (rounded to well-rounded soils), their φ_1^c, φ_2^c and φ_3^c values based on 2D images have a relative small variance range of 0.06, and are close to these values based on 3D images, with a maximum divergence of 0.04.

The φ_1^c, φ_2^c and φ_3^c values are used to compute the degrees of contact

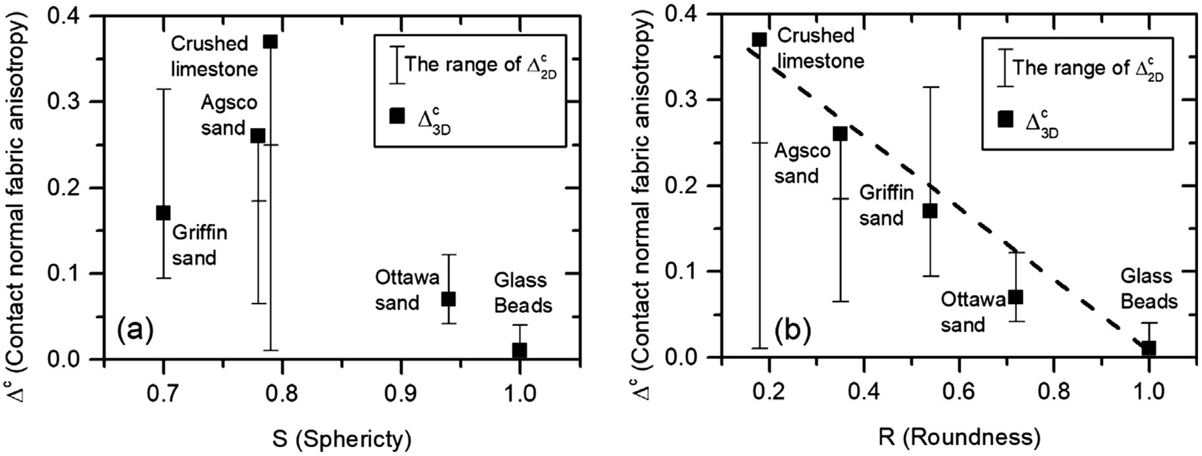

Fig. 15. The degrees of contact normal fabric anisotropy from 2D and 3D images and their relationships with soil sphericity and roundness.

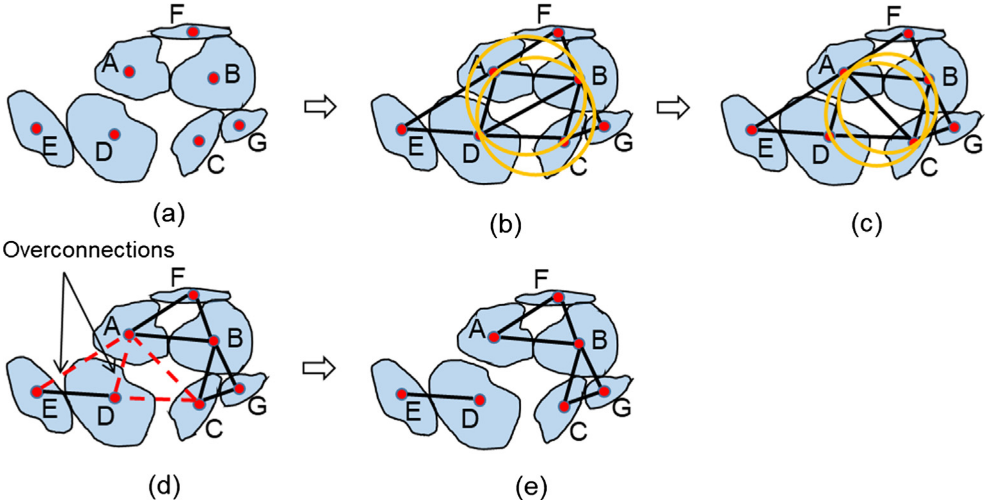

Fig. 16. Illustration of the modified Delaunay triangulation technique.

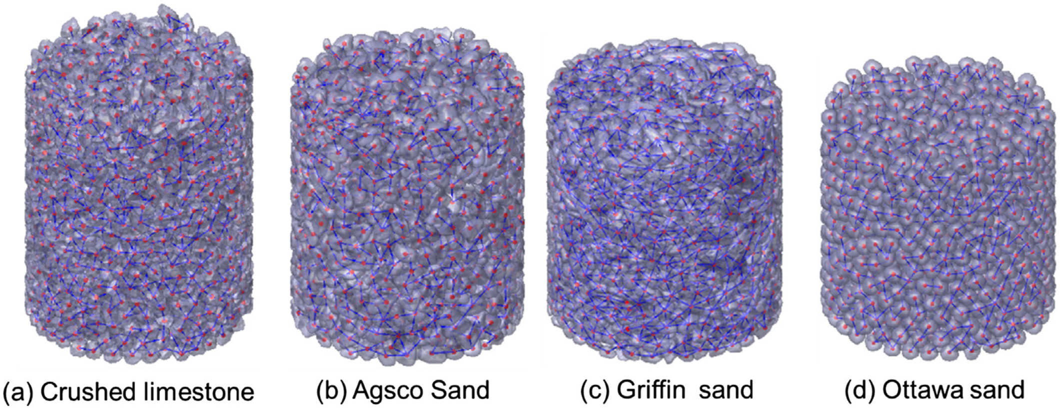
(a) Crushed limestone (b) Agsco Sand (c) Griffin sand (d) Ottawa sand

Fig. 17. Branch vectors in 3D images by the modified Delaunay triangulation.

normal fabric anisotropy (Δ^c) for five sands using Eq. (12). The results are plotted against sphericity and roundness values in Fig. 15. For crushed limestone, Agsco sand, and Griffin sand, the Δ^c_{2D} values have a large variance range due to the large variances of φ^c_1, φ^c_2 and φ^c_3 values from 2D images. For crushed limestone and Agsco sand, the Δ^p_{2D} values are smaller than Δ^p_{3D} values, suggesting that the results from 2D images would underestimate degree of contact normal fabric anisotropy in 3D sands with very angular to angular particles. For Ottawa sand and Glass beads with rounded to well-rounded particles, the Δ^c_{2D} values are close to Δ^c_{3D} values with a maximum divergence of 0.05.

In Fig. 15(b), the Δ^c_{3D} values decreases with increasing R values, suggesting angular sands tend to develop stronger contact normal fabric anisotropy. However, there is no decisive relationship observed between Δ^c_{3D} values and S values in Fig. 15(a).

The observations in Figs. 14 and 15 may be explained as follows. The interparticle contacts of granular soils are complicated, which include point-to-point contacts, point-to-surface contacts, point-to-edge contacts, surface-to-surface contacts, edge-to-surface contacts, and

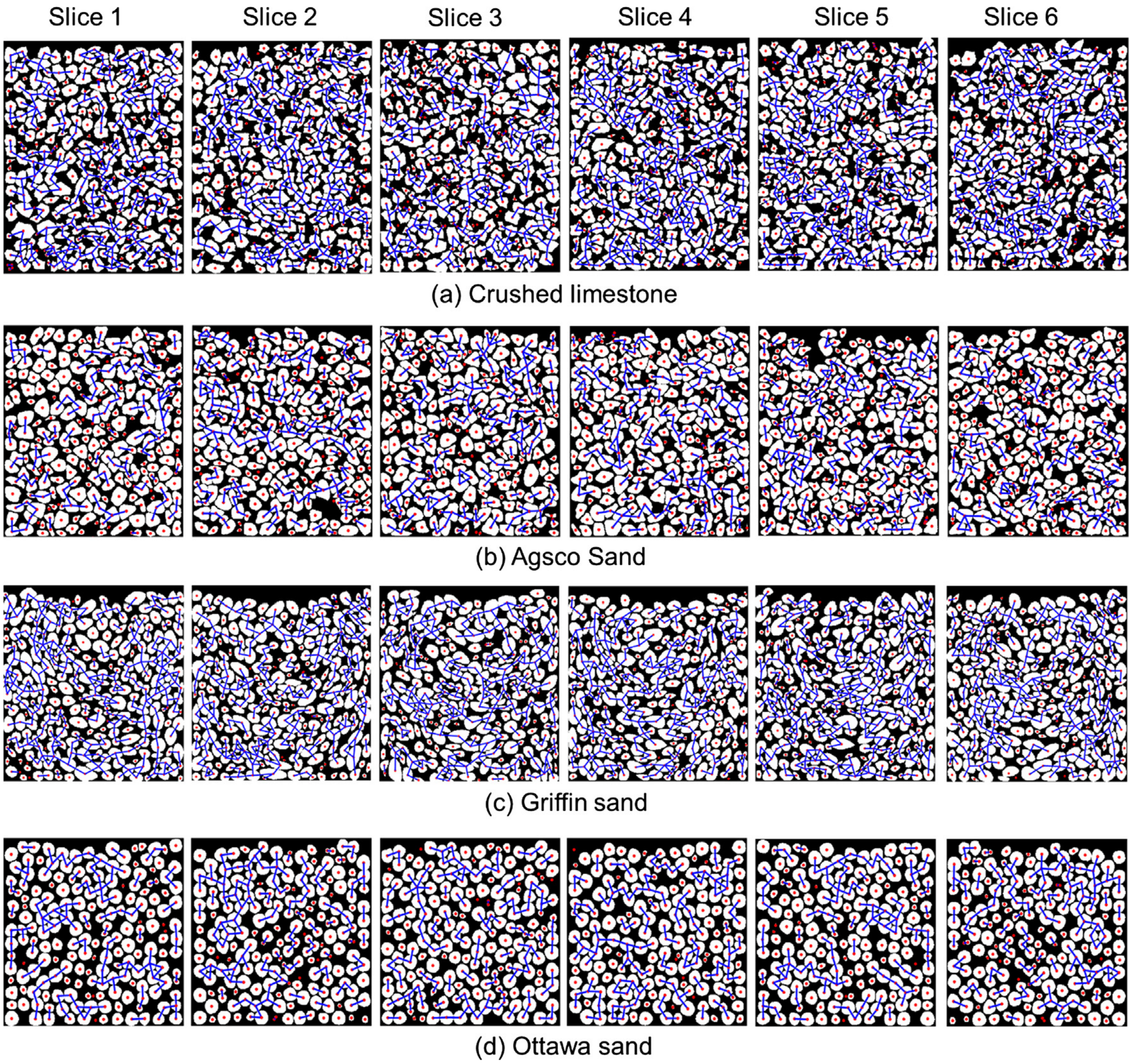

Fig. 18. Branch vectors in 2D images by the modified Delaunay triangulation.

edge-to-edge contacts. After cutting specimen vertically, the orientations of contact normals in 2D slices would be different to their actual 3D orientations, especially for point and edge related contacts (i.e., point-to-point, point-to-surface, point-to-edge, edge-to-surface, and edge-to-edge contacts). Very angular to sub-rounded sands may contain many point and edge related contacts. Therefore, a large variance range of Δ_{2D}^c values is observed for these sands. Rounded to well-rounded sands contain mainly face-to-face contacts and their contact normals are less affected in 2D slices. Therefore, Δ_{2D}^c values are within a small range, andΔ_{2D}^c and Δ_{3D}^c values are close for rounded and well-rounded sands.

In summary, contact normal fabric characterizations (φ_1^c, φ_2^c, φ_3^c, and Δ_{2D}^c values) determined from 2D images would have a large variance range for very angular to sub-rounded sands (most natural sands) and may underestimate contact normal fabric anisotropy in very angular to angular sands. This would result in a great uncertainty for using 2D images to estimate contact normal fabric anisotropy in 3D sand specimens.

For rounded to well-rounded sands (typically manufactured sands for special applications), contact normal fabric characterizations (φ_1^c, φ_2^c, φ_3^c, and Δ_{2D}^c values) determined from 2D images yield adequately accurate approximations to contact normal fabric anisotropy in 3D sand specimens.

4.3. Branch vector fabric anisotropy

A branch vector is a vector connecting the centroids of two contacting particles. The branch vectors only exist between contacting particles, such as particles M and N in Fig. 1. If the particles are not contacting, such as particles O and M or particles O and N, no branch vectors can be constructed. A modified Delaunay triangulation technique was developed by Sun and Zheng [22] to determine branch vectors in 3D and 2D images.

Six particles in Fig. 16(a) are used as an example to illustrate the Delaunay triangulation and modified Delaunay triangulation techniques. The Delaunay triangulation technique is applied to the centroids of particles to build a 2D mesh in Fig. 16(b). However, the triangular mesh may not be unique for a set of points. For example, points A, B, C, and D can construct two possible triangular meshes, as shown in Fig. 16(b) and (c). Therefore, Delaunay triangulation includes a criterion that circumcircles of triangles cannot contain any other points in their interiors. For example, in Fig. 16(b), the circumcircle of △ABD contains point C in its interior, and the circumcircle of △BCD contains point A in its interior. Therefore, the mesh in Fig. 16(b) is not satisfactory. In Fig. 16(c), circumcircles of △ABC and △ACD do not contain other points in their interiors. Therefore, both triangles meet the Delaunay criterion, and the mesh is satisfactory. The Delaunay criterion ensures the uniqueness of the mesh and ensures no skewed and irregular triangles are generated.

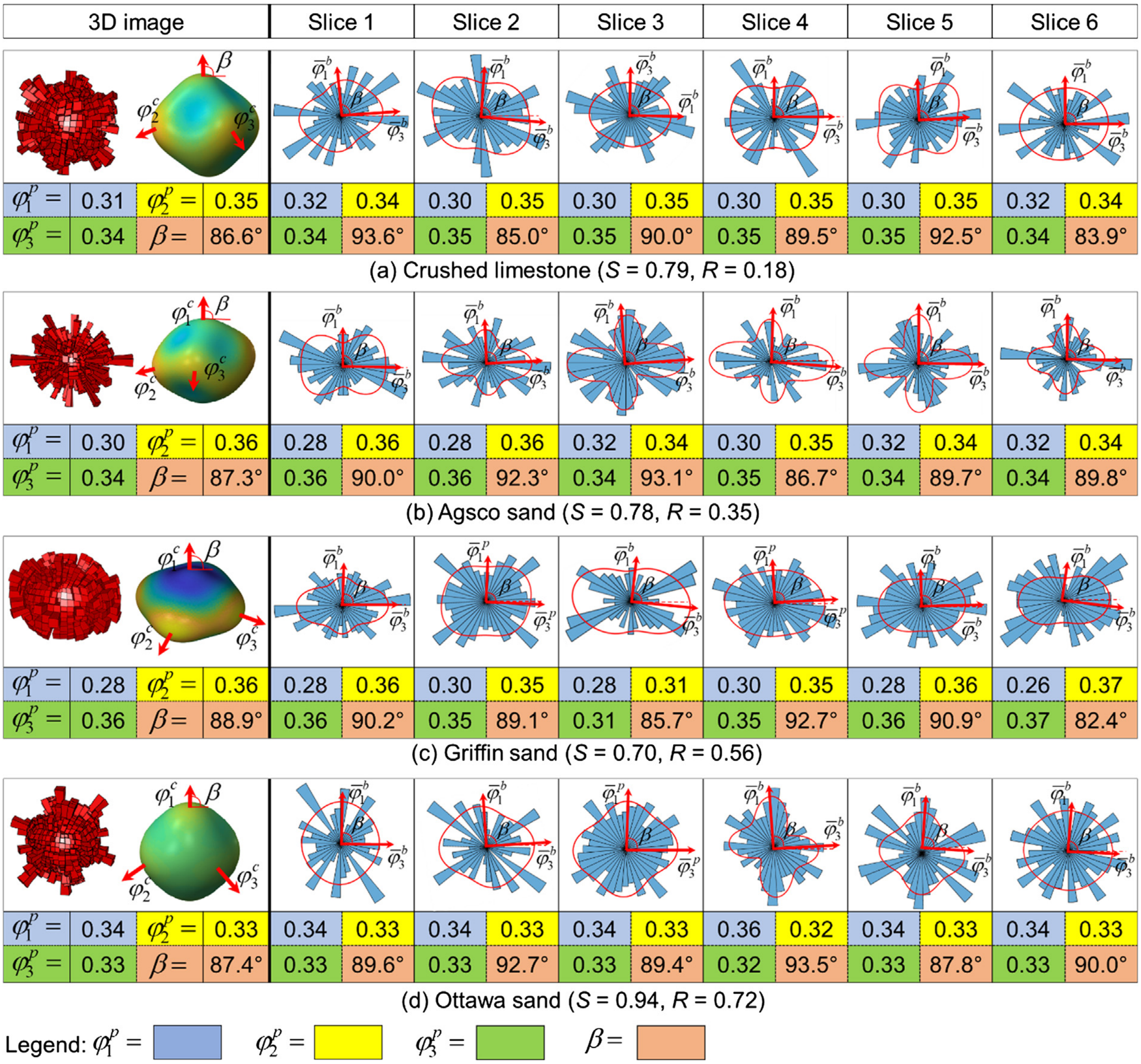

3D image				Slice 1		Slice 2		Slice 3		Slice 4		Slice 5		Slice 6	
$\varphi_1^p =$	0.31	$\varphi_2^p =$	0.35	0.32	0.34	0.30	0.35	0.30	0.35	0.30	0.35	0.30	0.35	0.32	0.34
$\varphi_3^p =$	0.34	$\beta =$	86.6°	0.34	93.6°	0.35	85.0°	0.35	90.0°	0.35	89.5°	0.35	92.5°	0.34	83.9°

(a) Crushed limestone (S = 0.79, R = 0.18)

$\varphi_1^p =$	0.30	$\varphi_2^p =$	0.36	0.28	0.36	0.28	0.36	0.32	0.34	0.30	0.35	0.32	0.34	0.32	0.34
$\varphi_3^p =$	0.34	$\beta =$	87.3°	0.36	90.0°	0.36	92.3°	0.34	93.1°	0.35	86.7°	0.34	89.7°	0.34	89.8°

(b) Agsco sand (S = 0.78, R = 0.35)

$\varphi_1^p =$	0.28	$\varphi_2^p =$	0.36	0.28	0.36	0.30	0.35	0.28	0.31	0.30	0.35	0.28	0.36	0.26	0.37
$\varphi_3^p =$	0.36	$\beta =$	88.9°	0.36	90.2°	0.35	89.1°	0.31	85.7°	0.35	92.7°	0.36	90.9°	0.37	82.4°

(c) Griffin sand (S = 0.70, R = 0.56)

$\varphi_1^p =$	0.34	$\varphi_2^p =$	0.33	0.34	0.33	0.34	0.33	0.34	0.33	0.36	0.32	0.34	0.33	0.34	0.33
$\varphi_3^p =$	0.33	$\beta =$	87.4°	0.33	89.6°	0.33	92.7°	0.33	89.4°	0.32	93.5°	0.33	87.8°	0.33	90.0°

(d) Ottawa sand (S = 0.94, R = 0.72)

Legend: $\varphi_1^p =$ 🟦 $\varphi_2^p =$ 🟨 $\varphi_3^p =$ 🟩 $\beta =$ 🟧

Fig. 19. Branch vector fabric characterizations based on 2D and 3D images.

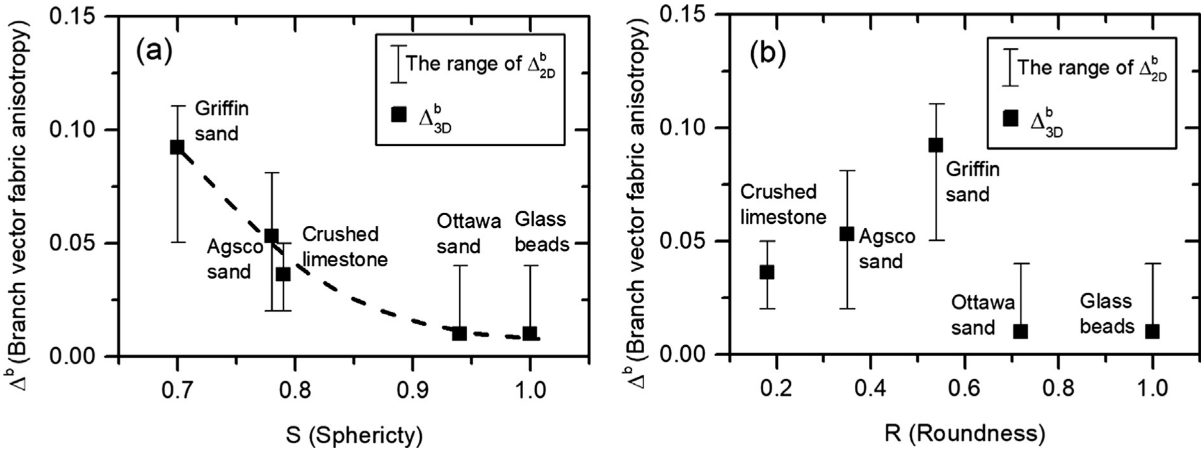

Fig. 20. The degree of branch vector fabric anisotropy from 2D and 3D images and their relationships with soil sphericity and roundness.

The particles A and D, A and E, A and C, and C and D are not contacting each other as shown in Fig. 16(d). Therefore, their centroid connections should not be branch vectors. These connections are defined as "overconnections", which should be eliminated from the mesh. The Delaunay triangulation technique cannot identify overconnections in the mesh. Therefore, Sun and Zheng [22] modified Delaunay triangulation to address this issue.

All the contacts and their associated particles have been identified in the improved watershed analysis. Therefore, this information is used here to evaluate whether contacts exist between two particles to search overconnections. After removing the overconnections, the branch vectors can be identified as shown in Fig. 16(e).

Delaunay triangulation can also be applied to points in 3D space to create a 3D mesh. Each mesh element was a tetrahedron consisting of four points. To ensure the uniqueness of the 3D mesh, the circumscribing sphere of each tetrahedron must not contain any other points in its interior. The contacts between 3D particles have been identified in the improved watershed analysis. The modified Delaunay triangulation can use this information to eliminate overconnections between 3D particles and determine branch vectors.

The modified Delaunay triangulation was used to analyze 3D and 2D images of four sands: crushed limestone, Agsco sand, Griffin sand, and Ottawa sand, to determine their branch vectors. The results are shown in Figs. 17 and 18. The branch vectors of glass beads are the same as the contact normals. Therefore, branch vectors of glass beads are not ploted in Fig. 17.

The branch vectors in 3D and 2D image are used to determine principal values (i.e. φ_1^b, φ_2^b, and φ_3^b), fabric direction (β), 3D rose diagram, and density function as shown in Fig. 19. The branch vectors display a preferred horizontal direction for crushed limestone, Agsco sand, and Griffin sand as that their φ_2^b and φ_3^b values are larger than φ_1^b, and rose diagrams and density functions are flat in the horizontal direction. The fabric direction β is close to 90°. The branch vectors in Ottawa sand and glass beads (the results of glass beads are shown in Fig. 14) display an isotropic fabric.

One would expect that branch vector and contact normal between two contacting particles should be aligned in a similar direction. Therefore, branch vector fabric characterizations should be similar to contact normal fabric characterizations. This is true if all the particles are spheres, but they have no decisive relationship in real soils consisting of irregular particles, because the contact normals of irregular particles could be any direction and not necessarily align with the branch vectors [10].

In Fig. 19, the φ_1^b, φ_2^b and φ_3^b values based on 2D images vary depending on slicing directions, but the variance range is small, within 0.04. The φ_1^b, φ_2^b and φ_3^b values based on 2D images are close to these values based on 3D images for four soils. The maximum divergences of φ_1^b, φ_2^b and φ_3^b values between 3D and 2D images are within 0.03.

The Δ_{3D}^b and Δ_{2D}^b values are plotted against sphericity and roundness in Fig. 20. As discussed before, the contact normal fabric of glass beads are the same as branch vector normal fabric. Therefore, the results of glass beads are also plotted in Fig. 20.

The Δ_{2D}^b values agree with Δ_{3D}^b values for the five sands analyzed in this study, with a maximum divergence of 0.05. The Δ_{3D}^b values decrease as increasing S values as shown in Fig. 20(a). There is no decisive relationship observed between Δ_{3D}^b values and R values in Fig. 20(b).

In summary, the results in Figs. 19 and 20 show that branch vector fabric determined from 2D images yield adequately accurate approximations to branch vector fabric in 3D sand specimens.

5. Conclusion

This study used both 3D and 2D images to characterize inherent long axis fabric, contact normal fabric, and branch vector fabric in five sands. These sand specimens were prepared by air-pluviated method and were prepared at the same relative density of 85%.

For long axis fabric and branch vector fabric, fabric characterizations (i.e., φ_1^p, φ_2^p and φ_3^p) by using 2D images vary in a small range for differnet slicing directions and they agree with these values computed from 3D images, with a maximum divergence of 0.03. The degrees of fabric anisotropy computed from 3D and 2D (i.e., Δ_{2D}^p and Δ_{3D}^p values) agree with each other with a maximum divergence of 0.05. Therefore, the 2D images provide adequate accuracy for estimating the long axis fabric and branch vector fabric anisotropy in 3D sands.

For contact normal fabric, the reliability of fabric characterizations (i.e., φ_1^p, φ_2^p and φ_3^p) by using 2D images depends on types of soils. For rounded to well-rounded sands, fabric characterizations (i.e., φ_1^c, φ_2^c and φ_3^c) by using 2D images vary a small range for different slicing directions and they agree with these values computed from 3D images with a maximum divergence of 0.05. Therefore, the 2D images provide adequate accuracy for estimating the contact normal fabric in 3D sands with rounded to well-rounded particles. However, for most natural soils with very angular to sub-rounded particles, contact fabric characterizations (i.e., φ_1^c, φ_2^c and φ_3^c) by using 2D images would vary a large range and would possibly underestimate the contact normal fabric in 3D sands. It contains a great uncertainty to use 2D images to estimate contact normal fabric in 3D sands with very angular to subrounded particles.

It has been well-established that particle shape significantly affects macro-mechanical behavior of granular soils. This study analyzed the relationship between particle shape descriptors (i.e., sphericity and roundness) and degree of fabric anisotropy. We observed that sphericity impacts degrees of particle long axis fabric anisotropy Δ_{3D}^p and branch vector fabric anisotropy Δ_{3D}^b in sands. The Δ_{3D}^p and Δ_{3D}^b values increase as sphericity decrease, indicating elongated soils tend to develop stronger long axis fabric anisotropy and branch vector fabric anisotropy in sands. The roundness impacts degree of contact normal fabric anisotropy Δ_{3D}^c in sands. The Δ_{3D}^c values increase as roundness decrease, indicating angular soils tend to develop stronger contact normal fabric anisotropy in sands.

Acknowledgements

This material is based upon work supported by the U.S. National Science Foundation under Grant No. CMMI 1917332. Any opinions, findings, and conclusions or recommendations expressed in this material are those of the authors and do not necessarily reflect the views of the National Science Foundation.

References

[1] Zheng J, Hryciw RD. Particulate material fabric characterization by rotational haar wavelet transform. Comput Geotech 2017;88:46–60. https://doi.org/10.1016/j.compgeo.2017.02.021.

[2] Zheng J, Hryciw RD. Cross-anisotropic fabric of sands by wavelet-based simulation of human cognition. Soils Found 2018;58:1028–41. https://doi.org/10.1016/j.sandf.2018.06.001.

[3] Arthur JRFF, Menzies BK. Inherent anisotropy in a sand. Geotechnique 1972;22:115–28. https://doi.org/10.1680/geot.1973.23.1.128.

[4] Oda M. Initial fabric and their relations to mechanical properties of granular materials. Soils Found 1972;12:17–36.

[5] Tatsuoka F, Sakamoto M, Kawamura T, Fukushima S. Strength and deformation characteristics of sand in plane strain compression at extremely low pressures. Soils Found 1986;26:65–84. https://doi.org/10.3208/sandf1972.26.65.

[6] Guo P. Modified direct shear test for anisotropic strength of sand. J Geotech Geoenviron Eng 2008;134:1311–8. https://doi.org/10.1061/(asce)1090-0241(2008) 134:9(1311).

[7] Rodriguez NM, Lade PV. Non-coaxiality of strain increment and stress directions in cross-anisotropic sand. Int J Solids Struct 2014;51:1103–14. https://doi.org/10.1016/j.ijsolstr.2013.12.003.

[8] Azami A, Pietruszczak S, Guo P. Bearing capacity of shallow foundations in transversely isotropic granular media. Int J Numer Anal Meth Geomech 2009;34:771–93. https://doi.org/10.1002/nag.827.

[9] Bellotti R, Jamiolkowski M, Lo Presti DC, O'Neill DA. Anisotropy of small strain stiffness in Ticino sand. Geotechnique 1996;46:115–31.

[10] Fonseca J, O'Sullivan C, Coop MR, Lee PD. Quantifying the evolution of soil fabric during shearing using directional parameters. Géotechnique 2013;63:487–99. https://doi.org/10.1680/geot.12.P.003.

[11] Oda M, Nakayama H. Yield function for soil with anisotropic fabric. J Eng Mech 1989;115:89–104. https://doi.org/10.1061/(asce)0733-9399(1989) 115:1(89).

[12] Kuo C-YY, Frost JD, Chameau JLA. Image analysis determination of stereology based fabric tensors. Géotechnique 1998;48:515–25. https://doi.org/10.1680/geot.1998.48.4.515.

[13] Yang ZX, Li XS, Yang J. Quantifying and modelling fabric anisotropy of granular soils. Géotechnique 2008;58:237–48. https://doi.org/10.1680/geot.2008.58.4.237.

[14] Fonseca J, O'Sullivan C, Coop MR, Lee PD. Quantifying the evolution of soil fabric during shearing using scalar parameters. Géotechnique 2013;63:818–29. https://doi.org/10.1680/geot.11.P.150.

[15] Alam MF, Haque A, Ranjith PG. A study of the particle-level fabric and morphology of granular soils under one-dimensional compression using insitu X-ray CT imaging. Materials (Basel) 2018;11:16–8. https://doi.org/10.3390/ma11060919.

[16] Imseeh WH, Druckrey AM, Alshibli KA. 3D experimental quantification of fabric and fabric evolution of sheared granular materials using synchrotron micro-computed tomography. Granul Matter 2018;20:1–28. https://doi.org/10.1007/s10035-018-0798-x.

[17] Al Mahbub A, Haque A. X-ray computed tomography imaging of the microstructure of sand particles subjected to high pressure one-dimensional compression. Materials (Basel) 2016;9:7–15. https://doi.org/10.3390/ma9110890.

[18] Soriano I, Ibraim E, Andò E, Diambra A, Laurencin T, Moro P, et al. 3D fibre architecture of fibre-reinforced sand. Granul Matter 2017;19:1–14. https://doi.org/10.1007/s10035-017-0760-3.

[19] Druckrey AM, Alshibli KA, Al-Raoush RI. 3D characterization of sand particle-to-particle contact and morphology. Comput Geotech 2016;74:26–35. https://doi.org/10.1016/j.compgeo.2015.12.014.

[20] Wiebicke M, Andò E, Viggiani G, Herle I. Towards the measurement of fabric in granular materials with X-ray tomography. 6th int symp deform charact geomaterials, Buenos Aires, Argentinia. 2015.

[21] Wiebicke M, Ando E, Herle I, Viggiani G. On the metrology of interparticle contacts in sand from X-ray tomography images. Meas Sci Technol 2017;28. https://doi.org/10.1088/1361-6501/aa8dbf.

[22] Sun Q, Zheng J, He H, Li Z. Particulate material fabric characterization from volumetric images by computational geometry. Powder Technol 2019;344:804–13. https://doi.org/10.1016/j.powtec.2018.12.070.

[23] Lim K-WW, Kawamoto R, Andò E, Viggiani G, Andrade JE. Multiscale characterization and modeling of granular materials through a computational mechanics avatar: a case study with experiment. Acta Geotech 2015;11:243–53. https://doi.org/10.1007/s11440-015-0405-9.

[24] Alshibli KA, Jarrar MF, Druckrey AM, Al-Raoush RI. Influence of particle morphology on 3D kinematic behavior and strain localization of sheared sand. J Geotech Geoenviron Eng 2017;143:1–25. https://doi.org/10.1061/(asce)gt.1943-5606.0001601.

[25] Zhou B, Wang J. Random generation of natural sand assembly using micro X-ray tomography and spherical harmonics. Géotechnique Lett 2015;5:6–11. https://doi.org/10.1680/geolett.14.00082.

[26] Zhou B, Wang J. Generation of a realistic 3D sand assembly using X-ray micro-computed tomography and spherical harmonic-based principal component analysis. Int J Numer Anal Methods Geomech 2016;41:93–109. https://doi.org/10.1002/nag.2548.

[27] Kong D, Fonseca J. Quantification of the morphology of shelly carbonate sands using 3D images. Géotechnique 2018;68:249–61. https://doi.org/10.1680/jgeot.16.P.278.

[28] Masad E, Tashman L, Little D, Zbib H. Viscoplastic modeling of asphalt mixes with the effects of anisotropy, damage and aggregate characteristics. Mech Mater 2005;37:1242–56. https://doi.org/10.1016/j.mechmat.2005.06.003.

[29] Yao Y-P, Kong Y-X. Extended UH model: Three-dimensional unified hardening model for anisotropic clays. J Eng Mech 2012;138:853–66. https://doi.org/10.1061/(asce)em.1943-7889.0000397.

[30] Tong Z, Fu P, Zhou S, Dafalias YF. Experimental investigation of shear strength of sands with inherent fabric anisotropy. Acta Geotech 2014;9:257–75. https://doi.org/10.1007/s11440-014-0303-6.

[31] Cho G-C, Dodds J, Santamarina JC. Particle shape effects on packing density, stiffness, and strength: natural and crushed sands. J Geotech Geoenviron Eng 2006;132:591–602. https://doi.org/10.1061/(asce)1090-0241(2006) 132:5(591).

[32] Shin H, Santamarina JC. Role of particle angularity on the mechanical behavior of granular mixtures. J Geotech Geoenviron Eng 2013;139:353–5. https://doi.org/10.1061/(asce)gt.1943-5606.0000768.

[33] Alshibli KA, Cil MB. Influence of particle morphology on the friction and dilatancy of sand. J Geotech Geoenvironmental Eng 2018;144:04017118. https://doi.org/10.1061/(ASCE)GT.1943-5606.0001841.

[34] Zheng J, Hryciw RD, Ventola A. Compressibility of sands of various geologic origins at pre-crushing stress levels. Geol Geotech Eng 2017;35:2037–51. https://doi.org/10.1007/s10706-017-0225-9.

[35] Jerves AX, Kawamoto RY, Andrade JE. Effects of grain morphology on critical state: a computational analysis. Acta Geotech 2016;11:493–503. https://doi.org/10.1007/s11440-015-0422-8.

[36] Altuhafi FN, Coop MR, Georgiannou VN. Effect of particle shape on the mechanical properties of natural sands. J Geotech Geoenviron Eng 2016;142:1–15. https://doi.org/10.1061/(ASCE)GT.1943-5606.0001569.

[37] Liu X, Yang J. Shear wave velocity in sand: effect of grain shape. Géotechnique 2018;68:742–8. https://doi.org/10.1680/jgeot.17.t.011.

[38] Bareither CA, Edil TB, Benson CH, Mickelson DM. Geological and physical factors affecting the friction angle of compacted sands. J Geotech Geoenviron Eng 2008;134:1476–89. https://doi.org/10.1061/(asce)1090-0241(2008) 134:10(1476).

[39] Zheng J, Hryciw RD. Index void ratios of sands from their intrinsic properties. J Geotech Geoenviron Eng 2016;142:06016019. https://doi.org/10.1061/(ASCE)GT.1943-5606.0001575, 06016019.

[40] Kandasami R, Murthy T. Effect of particle shape on the mechanical response of a granular ensemble. Geomech from Micro to Macro, Informa UK Limited 2014. p. 1093–8. https://doi.org/10.1201/b17395-196.

[41] Nouguier-Lehon C, Cambou B, Vincens E. Influence of particle shape and angularity on the behaviour of granular materials: a numerical analysis. Int J Numer Anal Methods Geomech 2003;27:1207–26. https://doi.org/10.1002/nag.314.

[42] Vangla P, Roy N, Gali ML. Image based shape characterization of granular materials and its effect on kinematics of particle motion. Granul Matter 2017;20. https://doi.org/10.1007/s10035-017-0776-8.

[43] Cavarretta I, Coop M, O'Sullivan C. The influence of particle characteristics on the behaviour of coarse grained soils. Géotechnique 2010;60:413–23. https://doi.org/10.1680/geot.2010.60.6.413.

[44] Satake M. Fabric tensor in granular materials. In: Vermeer PA, Luger HJ, editors. IUTAM symp deform fail granul mater. Rotterdam (Netherlands): Balkema; 1982. p. 63–8.

[45] Kanatani K. Distribution of directional data and fabric tensors. Int J Eng Sci 1984;22:149–64.

[46] Dafalias YF, Papadimitriou AG, Li XS. Sand plasticity model accounting for inherent fabric anisotropy. J Eng Mech 2004;130:1319–33. https://doi.org/10.1061/(asce)0733-9399(2004) 130:11(1319).

[47] Dafalias YF, Li XS, Dafalias YF. A constitutive framework for anisotropic sand including non-proportional loading. Géotechnique 2004;54:41–55. https://doi.org/10.1680/geot.54.1.41.36329.

[48] Gao Z, Zhao J, Yao Y. A generalized anisotropic failure criterion for geomaterials. Int J Solids Struct 2010;47:3166–85. https://doi.org/10.1016/j.ijsolstr.2010.07.016.

[49] Gao Z, Zhao J. Strain localization and fabric evolution in sand. Int J Solids Struct 2013;50:3634–48. https://doi.org/10.1016/j.ijsolstr.2013.07.005.

[50] Zhao J, Gao Z. Unified anisotropic elastoplastic model for sand. J Eng Mech 2016;142:04015056. https://doi.org/10.1061/(ASCE)EM.1943-7889.0000962.

[51] Zhao J, Guo N. Unique critical state characteristics in granular media considering fabric anisotropy. Géotechnique 2013;63:695–704. https://doi.org/10.1680/geot.12.p.040.

[52] Guo N, Zhao J. The signature of shear-induced anisotropy in granular media. Comput Geotech 2013;47:1–15. https://doi.org/10.1016/j.compgeo.2012.07.002.

[53] Huang X, Hanley KJ, O'Sullivan C, Kwok CY. Exploring the influence of interparticle friction on critical state behaviour using DEM. Int J Numer Anal Methods Geomech 2014;38:1276–97. https://doi.org/10.1002/nag.2259.

[54] Huang X, O'Sullivan C, Hanley KJ, Kwok CY. Discrete-element method analysis of the state parameter. Géotechnique 2014;64:954–65. https://doi.org/10.1680/geot.14.P.013.

[55] Barreto D, O'Sullivan C. The influence of inter-particle friction and the intermediate stress ratio on soil response under generalised stress conditions. Granul Matter 2012;14:505–21. https://doi.org/10.1007/s10035-012-0354-z.

[56] Otsu N. A threshold selection method from gray-level histograms. IEEE Trans Syst Man Cybern 1979;9:62–6.

[57] Alam MF, Haque A. A new cluster analysis-marker-controlled watershed method for separating particles of granular soils. Materials (Basel) 2017;10. https://doi.org/10.3390/ma10101195.

[58] Zheng J, Hryciw RD. Segmentation of contacting soil particles in images by modified watershed analysis. Comput Geotech 2016;73:142–52. https://doi.org/10.1016/j.compgeo.2015.11.025.

[59] Krumbein WC, Sloss LL. Stratigraphy and sedimentation. San Francisco: W.H. Freeman and Company; 1951.

[60] Wadell H. Volume, shape, and roundness of rock particles. J Geol 1932;40:443–51. https://doi.org/10.1086/623964.

[61] Wadell H. Sphericity and roundness of rock particles. J Geol 1933;41:310–31. https://doi.org/10.1086/624040.

[62] Wadell H. Volume, shape, and roundness of quartz particles. J Geol 1935;43:250–80. https://doi.org/10.1086/624298.

[63] Zheng J, Hryciw RD. Traditional soil particle sphericity, roundness and surface roughness by computational geometry. Géotechnique 2015;65:494–506. https://doi.org/10.1680/geot.14.P.192.

[64] Zheng J, Hryciw RD. Roundness and sphericity of soil particles in assemblies by computational geometry. J Comput Civ Eng 2016;30:1–13. https://doi.org/10.1061/(ASCE)CP.1943-5487.0000578, 04016021.

[65] Lade PV, Rodriguez NM, Van Dyck EJ. Effects of principal stress directions on 3D failure conditions in cross-anisotropic sand. J Geotech Geoenviron Eng 2014;140:1–12. https://doi.org/10.1061/(ASCE)GT.1943-5606.0001005.

[66] Oda M. Anisotropic strength of cohesionless sands. J Geotech Eng Div 1981;107:1219–31.